

Mathematical Model for Decarburization of Ultra-low Carbon Steel in Single Snorkel Refining Furnace

ZHIMIN YOU, GUOGUANG CHENG, XINCHAO WANG, ZHE QIN, JUN TIAN,
and JIAN ZHANG

A dynamic model is developed to investigate decarburization behavior of a new type of refining equipment named Single Snorkel Refining Furnace (SSRF) in treating ultra-low carbon steel. Decarburization reactions in SSRF are considered to take place at three sites: Ar bubble surface, the bulk steel, and the bath surface. With the eccentricity of the porous plug (r_e/R_S) and the ratio of the snorkel diameter to the ladle diameter (D_S/D_L) of SSRF confirmed, circulation flow rate of molten steel is obtained through combined effects of vacuum pressure and gas flow rate. Besides, variation of the steel temperature is simulated associated with generated reaction heat and heat losses. The variation of \bar{C} concentration with treatment time is divided into three stages in accordance with decarburization rates and the simulated \bar{C} concentration is in reasonable agreement with actual production data. In the present study, both decarburization rates at three sites and their contributions to the overall decarburization at each stage are estimated for the first time. Through the present investigation, it is clear that vacuum pressure significantly influences decarburization efficiency of SSRF primarily by affecting the depth of CO nucleation in the bulk steel. Besides, effects of gas flow rate on decarburization rate of different stages are obtained and the opportunity of increasing gas flow rate during the treatment period has been clarified. The present model provides an efficient tool to comprehend the decarburization process in SSRF.

DOI: 10.1007/s11663-014-0182-0

© The Minerals, Metals & Materials Society and ASM International 2014

I. INTRODUCTION

IN recent years, with the increasing demand for ultra-low carbon steel, improving carbon removal efficiency is becoming more and more important in the refining process. Currently, RH degasser has been worldwide applied and shown good decarburization performance in the production of ultra-low carbon steel.^[1–3] However, the life cycle of immersed snorkels refractory and vacuum vessel refractory is short in RH due to severe erosion caused by steel circulation, gas blowing, and violent steel splashing. Single Snorkel Refining Furnace (SSRF) is a new-type refining equipment with simple configurations,^[4] in which a large snorkel is immersed into molten steel of the ladle and Ar gas is eccentrically injected into molten steel from the ladle bottom, as shown in Figure 1. Interestingly, molten steel circulates rapidly with little steel splashing in the vacuum vessel of SSRF, because the flow rate of Ar gas for stirring the melt is relatively low due to long gas ascending distance within the steel. Therefore, the life cycle of vacuum vessel is greatly prolonged compared to RH degasser.^[5]

Now SSRF has been used for decarburization, degassing, desulphurization, deoxidation, alloying, adjusting chemical compositions and inclusions removal from molten steel, *etc.*^[6] Up to now, various correlative investigations on SSRF have been made. Cheng *et al.*^[7] put forward a dynamic model to investigate deoxidation rate for bearing steel and the mass transfer constant of deoxidation was determined based on over 100 heats industrial tests in a 35-ton SSRF. Then a deoxidation process was proposed, through which the oxygen concentration of bearing steel can be limited to a range from 10 to 20 ppm.^[8] Besides, a critical gas flow rate was confirmed through investigation of slag entrainment process in SSRF.^[9] Bubble behavior and effect of gas flow rate and porous diameter on mixing time of SSRF were also studied based on a physical model with a scale factor of 1:4.^[10] In addition, Yang *et al.*^[11] made a mathematical simulation of flow field for molten steel in an 80-ton SSRF, through which reasonable gas flow rate, eccentric position of bottom blowing Ar gas, inner diameter, and immersion depth of the single snorkel were obtained. Recently, a mathematical model has been established by Rui *et al.*^[12] to investigate desulphurization behavior in SSRF, in which the desulphurization rate constant ($1.0E-8$) was confirmed. Besides, physical model experiments have been performed to investigate effect of elliptical snorkel on decarburization in SSRF and comparison between elliptical snorkel and round snorkel was also made.^[13] Based on industrial tests^[14] in an 80-ton SSRF of Shanxi Taigang Stainless Steel Corporation Limited, the maximum desulphurization

ZHIMIN YOU, Master Student, GUOGUANG CHENG and JIAN ZHANG, Professors, XINCHAO WANG, Master Student, and ZHE QIN and JUN TIAN, Doctoral Students, are with the State Key Laboratory of Advanced Metallurgy, and School of Metallurgical and Ecological Engineering, University of Science and Technology Beijing, Beijing 100083, P.R. China. Contact e-mail: yzm2008beijing@126.com

Manuscript submitted July 31, 2013.

Article published online September 9, 2014.

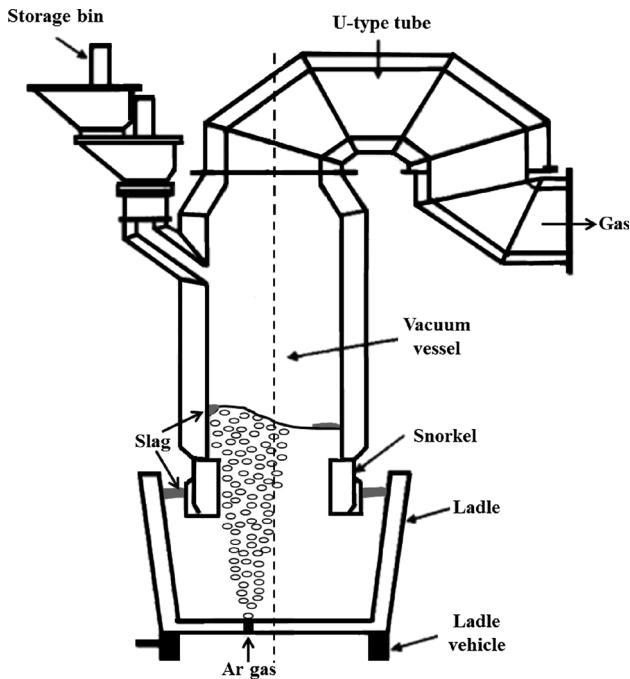
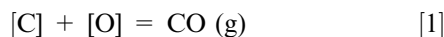


Fig. 1—Schematic illustration of Single Snorkel Refining Furnace (SSRF).

ratio of 81.2 pct has been achieved and the sulfur content of molten steel can be reduced to about 10 ppm. Likewise, the terminal carbon content of 10 ppm has also been achieved in the industrial decarburization tests^[15] within 20 min. Although the results of decarburization tests in SSRF have shown good performance in treating ultra-low carbon steel, the terminal carbon concentration of molten steel fluctuates widely^[15] and decarburization mechanism of SSRF has been little reported at present. In order to further improve decarburization efficiency in treating ultra-low carbon steel and provide probable guidance for industrial scale production in SSRF, a dynamic model will be developed to investigate decarburization behavior of SSRF in the present study. Confirmation of decarburization rate of each reaction site will be explained in detail and effects of process parameters (vacuum pressure, gas flow rate, concentration of \underline{C} , \underline{O}) on decarburization rate of SSRF will be also explained.

II. DESCRIPTION OF THE MATHEMATICAL MODEL

The decarburization reaction in SSRF can be expressed by Eq. [1].



In above reaction, the equilibrium constant K of can be calculated as follows.^[16]

$$K = \frac{P_{CO}/P^\theta}{f_C \cdot [\text{pct } C] \cdot f_O \cdot [\text{pct } O]} = 10^{\frac{1160}{T_{\text{melt}}} + 2.003} \quad [2]$$

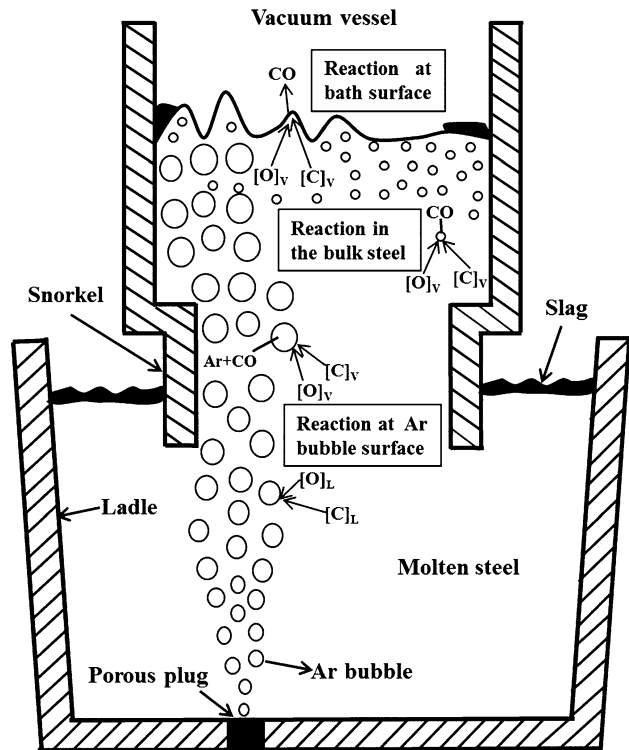


Fig. 2—Schematic diagram of decarburization mechanism of each site in SSRF.

As shown in Eq. [2], K depends on the temperature of molten steel (T_{melt}). When T_{melt} is known, equilibrium CO partial pressure is determined by equilibrium concentration of \underline{C} , \underline{O} .

A. Decarburization Reaction Sites

In the present study, it is assumed that decarburization reactions take place at three sites in SSRF: Ar bubble surface, the bulk steel, and the bath surface. Figure 2 depicts the schematic diagram of decarburization mechanism of each reaction site in SSRF. Ar bubble surface decarburization occurs under the circumstance of dissolved \underline{C} , \underline{O} transferring to the interface, and then generated \overline{CO} gas transfers into Ar bubble. This process proceeds continuously during a bubble rising from the porous plug to the bath surface. Meanwhile, when vacuum pressure drops to a certain level, large numbers of small CO bubbles will be formed in the bulk steel and then ascend into the vacuum chamber. Besides, the bath surface updates rapidly with gas stirring the melt violently and evacuating the vacuum vessel, which largely promotes decarburization reaction here. Once CO gas is formed at the bath surface, it gets into the gas phase and is soon exhausted out of vacuum vessel together with Ar gas. Obviously, both bath surface decarburization and bulk steel decarburization only occur in the vacuum vessel. However, Ar bubble surface decarburization takes place not only in the vacuum vessel but also in the ladle. In this model, each decarburization is investigated separately and then

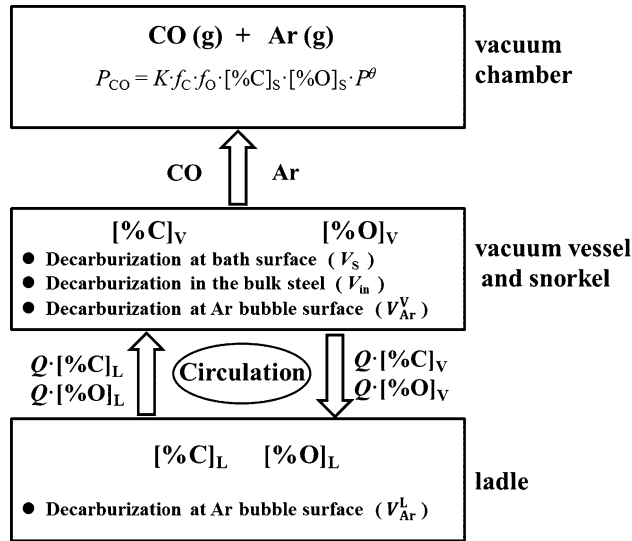


Fig. 3—Material balance in the decarburization process of SSRF.

the total decarburization amount is calculated by summing that of each reaction site.

B. Formulation of Decarburization Process in SSRF

The concept of this model can be described as follows: \underline{C} concentration of molten steel in the vacuum vessel differs from that in the ladle during the decarburization period because of different decarburization distributions between these two zones. However, dissolved \underline{C} , \underline{O} is assumed to be distributed evenly in both ladle and vacuum vessel; the very small difference of \underline{C} concentration between the ladle and the vacuum vessel maintains relatively stable with continuous circulation and mixing of molten steel.

Figure 3 depicts material balance in the decarburization process of SSRF. Equations [3] to [6] represent mass balance of \underline{C} , \underline{O} of the ladle and the vacuum vessel. The relationship among concentration of \underline{C} , \underline{O} , and equilibrium CO partial pressure is expressed by Eq. [7].

$$W(d[\text{pct C}]_L/dt) = Q([\text{pct C}]_V - [\text{pct C}]_L) - 100 \times V_{\text{Ar}}^L \quad [3]$$

$$W(d[\text{pct O}]_L/dt) = Q([\text{pct O}]_V - [\text{pct O}]_L) - 100 \times V_{\text{Ar}}^L \times \frac{M_{\text{O}}}{M_{\text{C}}} \quad [4]$$

$$w(d[\text{pct C}]_V/dt) = Q([\text{pct C}]_L - [\text{pct C}]_V) - 100 \times (V_{\text{Ar}}^V + V_{\text{in}} + V_{\text{s}}) \quad [5]$$

$$w(d[\text{pct O}]_V/dt) = Q([\text{pct O}]_L - [\text{pct O}]_V) - 100 \times (V_{\text{Ar}}^V + V_{\text{in}} + V_{\text{s}}) \times \frac{M_{\text{O}}}{M_{\text{C}}} \quad [6]$$

$$\log(f_{\text{C}} \cdot [\text{pct C}]^e \cdot f_{\text{O}} \cdot [\text{pct O}]^e \cdot P^{\theta} / P_{\text{CO}}) = -(1160/T_{\text{melt}} + 2.003) \quad [7]$$

C. Decarburization at Ar Bubble Surface

Injected Ar gas exists in the form of gas plume in molten steel. It has large superficial area for decarburization reaction. Low CO partial pressure in Ar bubbles significantly contributes to decarburization reaction at the interface. Decarburization through Ar bubbles involves such steps: dissolved \underline{C} , \underline{O} transferring from the melt to Ar bubble surface; chemical reaction at Ar bubble surface; and mass transfer of generated CO into Ar bubbles. According to reports^[17–20] on decarburization rate-determining step in RH, only when $[\text{pct O}]/[\text{pct C}] < 16/12$, may decarburization rate be controlled by mass transfer of dissolved \underline{O} , while $[\text{pct O}]$ is typically higher than $[\text{pct C}]$ during the decarburization period of SSRF, so influence of mass transfer of dissolved \underline{O} can be ignored comparing with that of dissolved \underline{C} on decarburization rate. In addition, mass transfer of \underline{CO} makes no resistance against the overall mass transfer due to very low CO partial pressure in the bubbles. Furthermore, chemical reaction proceeds rapidly under the high-temperature of molten steel. As decarburization principle of SSRF is similar to that of RH, mass transfer of dissolved \underline{C} to the interface is assumed to be the rate-determining step of Ar bubble surface decarburization in this model. Besides, Ar bubbles are assumed to be globular and do not coalesce in the ascending process. In the present study, decarburization reactions through Ar bubbles in the ladle and the vacuum vessel are separately estimated.

Reaction rate (mass percent/s) through Ar bubbles in the ladle is expressed by Eq. [8].

$$-\frac{d[\text{pct C}]_{\text{Ar}}^L}{dt} = \sum_{m=1}^{N_L} \frac{A_{\text{Ar}}^m \cdot \rho_m k_b}{W} ([\text{pct C}]_L - [\text{pct C}]_L^{\text{em}}), \quad [8]$$

where equilibrium \underline{C} concentration at Ar bubble surface of the ladle is calculated as follows.

$$[\text{pct C}]_L^{\text{em}} = \frac{P_{\text{CO,b}}^m}{K \cdot f_{\text{C}} \cdot f_{\text{O}} \cdot [\text{pct O}]_L \cdot P^{\theta}} \quad [9]$$

Reaction rate (mass percent/s) through Ar bubbles in the vacuum vessel is expressed by Eq. [10].

$$-\frac{d[\text{pct C}]_{\text{Ar}}^V}{dt} = \sum_{n=1}^{N_V} \frac{A_{\text{Ar}}^n \cdot \rho_n k_b}{w} ([\text{pct C}]_V - [\text{pct C}]_V^{\text{en}}), \quad [10]$$

where equilibrium \underline{C} concentration at bubble surface of the vacuum vessel is calculated as follows.

$$[\text{pct C}]_V^{\text{en}} = \frac{P_{\text{CO,b}}^n}{K \cdot f_{\text{C}} \cdot f_{\text{O}} \cdot [\text{pct O}]_V \cdot P^{\theta}} \quad [11]$$

As shown in Eqs. [9] and [11], equilibrium \underline{C} concentration decreases with the decrease of \underline{CO} partial

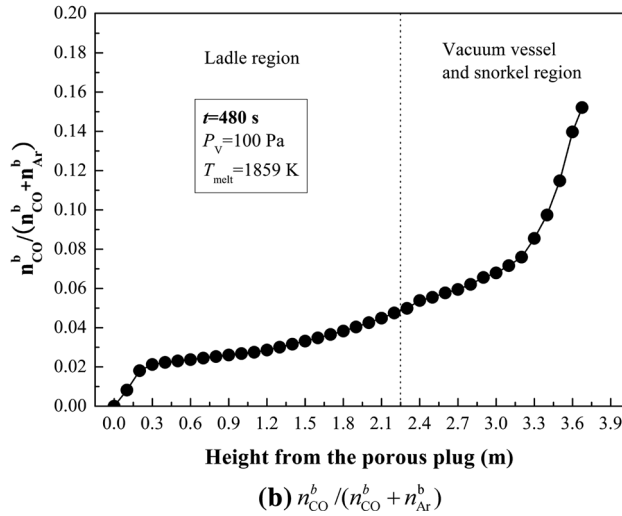
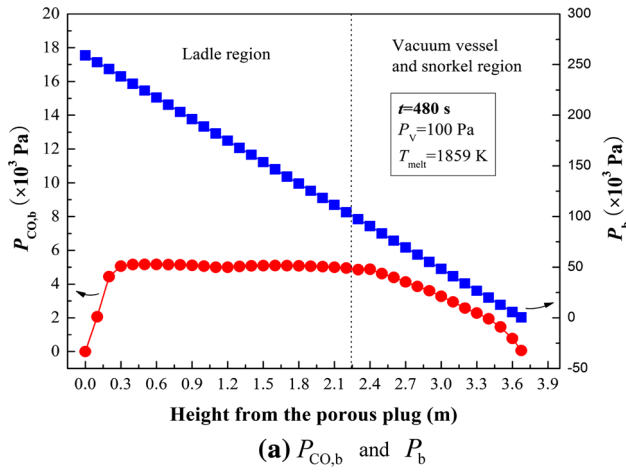


Fig. 4—Variations of $P_{CO,b}$, P_b , and $n_{CO}^b/(n_{CO}^b + n_{Ar}^b)$ with height from the porous plug ($t = 480$ s).

pressure. Hence, reduction of CO partial pressure enhances decarburization reaction at Ar bubble surface.

1. CO partial pressure in Ar bubble

Without regarding for CO making resistance against the overall mass transfer, CO partial pressure at the interface is assumed to be equal to CO partial pressure in Ar bubble, as shown in Eq. [12].

$$P_{CO,b} = \frac{n_{CO}^b}{n_{Ar}^b + n_{CO}^b} \times P_b \quad [12]$$

Here, n_{CO}^b is determined by the total decarburization amount within the risen distance of the estimated Ar bubble, and P_b can be calculated by Eq. [13].

$$P_b = \rho_m g h_b + P_v + \frac{2\sigma}{r_b} \quad [13]$$

According to calculations of Eqs. [12] and [13], variations of $P_{CO,b}$ and P_b , and the mole fraction of CO in Ar bubble ($n_{CO}^b/(n_{CO}^b + n_{Ar}^b)$) with height from the porous plug at $t = 480$ seconds are depicted in Figure 4.

As shown in Figure 4(a), $P_{CO,b}$ increases immediately when Ar gas is injected into molten steel, from which it can be inferred that Ar bubble surface decarburization takes place as soon as Ar gas enters molten steel. In a while, $P_{CO,b}$ increases to approximately 5000 Pa and remains stable until the bubbles escape from the ladle to the snorkel even if $n_{CO}^b/(n_{CO}^b + n_{Ar}^b)$ is still increasing as shown in Figure 4(b), because P_b drops constantly as it ascends in molten steel and its drop rate is almost equal to the rate of increase in $n_{CO}^b/(n_{CO}^b + n_{Ar}^b)$. However, when Ar bubbles are ascending in the vacuum vessel, a typical decrease tendency of $P_{CO,b}$ appears though $n_{CO}^b/(n_{CO}^b + n_{Ar}^b)$ increases more significantly. This can be ascribed to gradual increase of $\Delta P_b/P_b$ within the same height.

2. Mass transfer coefficient of dissolved carbon

For Ar bubble surface decarburization, mass transfer coefficients of dissolved C to the interface are calculated by Eq. [14] on the basis of solute penetration theory from Higbie.^[21]

$$k_b = 2 \left(\frac{D_C \cdot u_{slip}}{2\pi \cdot r_b} \right)^{1/2}, \quad [14]$$

where relative velocity of bubble (u_{slip}) is calculated by Eq. [15]^[22]

$$u_{slip} = \left(\frac{4\sigma^2 g}{\alpha \rho_m \mu} \times \frac{(\rho_m - \rho_g)}{\rho_m} \right)^{1/5} \quad [15]$$

3. Reaction area of Ar bubble surface decarburization

In this model, decarburization reaction taking place at every single Ar bubble surface is estimated and their sum is calculated as the total decarburization amount through Ar bubbles. Reaction area of a single bubble is obtained by Eq. [16].

$$A_{Ar}^p = 4\pi(r_b^p)^2 \quad [16]$$

According to investigation by Sano *et al.*^[23] on bubble formation at single-hole porous plug, the diameter of Ar bubble at the hole-outlet ($d_{b,0}$) can be calculated by Eq. [17].

$$d_{b,0} = \left[\left(\frac{6\sigma' d_0'}{\rho_m' g'} \right)^2 + \left\{ 0.54 \left(G'_{Ar} d_0'^{0.5} \right)^{0.289} \right\}^6 \right]^{1/6} \quad [17]$$

In terms of multi-hole porous plug, the gas flow rate through single-hole is equal distribution of the total gas to all the holes. Hence, $d_{b,0}$ at multi-hole porous plug can be obtained by Eq. [18].

$$d_{b,0} = \left[\left(\frac{6\sigma' d_0'}{\rho_m' g'} \right)^2 + \left\{ 0.54 \left(\frac{G'_{Ar}}{N_h} d_0'^{0.5} \right)^{0.289} \right\}^6 \right]^{1/6} \quad [18]$$

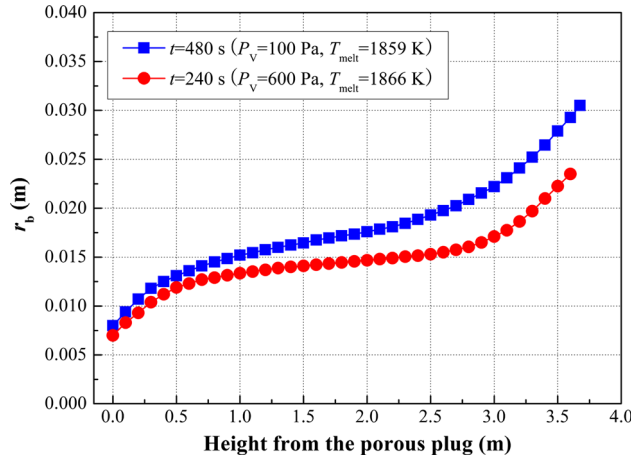


Fig. 5—Variations of Ar bubble radius with height from the porous plug ($t = 240, 480$ s).

It can be seen from Eq. [18] that $d_{b,0}$ depends on G'_{Ar}/N_b . In the present study, $d_{b,0}$ ranges from 1.4 to 1.6 cm due to variation of G'_{Ar} . On the basis of Szekely's^[24] study on bubble growth under reduced pressure, effect of the bubble temperature (T) on bubble growth is also taken into account in this model, as expressed by Eq. [19].

$$r_b'' + \frac{3r_b'^2}{2r_b} = \frac{1}{\rho_m r_b} \left[P_0 \left(\frac{r_{b,0}}{r_b} \right)^3 \cdot \frac{T}{T_0} - P_0 + \rho_m g u_b t_b \right] \quad [19]$$

$$P_0 = P_V + \rho_m g H_m; (t_b = 0; r_b = r_{b,0}, r_b' = 0)$$

In Eq. [19], T is determined according to the heat transfer from molten steel to Ar bubble as shown in Eq. [20].^[25]

$$\rho_g \cdot C_g \cdot V_g \cdot \frac{dT}{dt} = \psi \cdot A_{Ar}^p \cdot (T_{melt} - T) \quad [20]$$

According to Eqs. [18] and [19], the size of bubble is mainly influenced by G'_{Ar} , P_V , and T . Figure 5 depicts variations of bubble radius (r_b) with height from the porous plug at $t = 240$ seconds and $t = 480$ seconds.

It can be easily seen from Figure 5 that r_b increases with the increase of height from the porous plug, which is primarily ascribed to the reduction of hydrostatic pressure on Ar bubbles. Interestingly, r_b increases fast within the height of 0.5 m. This is probably caused by heat transfer from the melt to Ar bubbles and the reduction of hydrostatic pressure as well. r_b ranges from 0.007 to 0.0235 m at $t = 240$ seconds and from 0.016 to 0.061 m at $t = 480$ seconds. In terms of Ar bubbles of the same height, r_b at $t = 480$ seconds is bigger than that at $t = 240$ seconds, because the former P_V (600 Pa) is lower than the latter P_V (100 Pa).

4. Decarburization rate at Ar bubble surface

Based on the above calculations, decarburization rate through Ar bubbles in the ladle and the vacuum vessel can be obtained. The total decarburization rate (kg/s) at

Ar bubble surface is determined by the sum of decarburization rate of these two parts as shown in Eq. [21].

$$\left. \begin{aligned} V_{Ar}^L &= \left(-\frac{d[\text{pct C}]_{Ar}^L}{100 \cdot dt} \right) \times W \\ V_{Ar}^V &= \left(-\frac{d[\text{pct C}]_{Ar}^V}{100 \cdot dt} \right) \times w \end{aligned} \right\} V_{Ar} = V_{Ar}^L + V_{Ar}^V \quad [21]$$

D. Decarburization in the Bulk Steel

Decarburization in the bulk steel takes place when equilibrium CO partial pressure ($P_{CO,in}$) exceeds the sum of hydrostatic pressure of molten steel (P_h), vacuum pressure (P_V), and evolution pressure of CO bubbles (P_S). Therefore, the requirement for CO formation in the bulk steel can be expressed by Eq. [22].

$$P_{CO,in} \geq P_h + P_V + P_S \quad [22]$$

Bulk steel decarburization is very unlikely to occur through homogeneous nucleation of CO bubbles in a molten steel system, in which an astonishingly large gas super-saturation pressure of about 10^3 atm is required. Instead, heterogeneous nucleation of CO bubbles from small cavities of refractory surface becomes energetically feasible at a very small super-saturation pressure.^[26] The heterogeneous nucleation rate of CO bubbles in the bulk steel is in proportion to the difference between $P_{CO,in}$ and $P_h + P_V + P_S$. $P_{CO,in}$ ($= K \cdot f_C \cdot f_O \cdot [\text{pct C}]_V \cdot [\text{pct O}]_V$) mainly depends on $[\text{pct C}]_V$, $[\text{pct O}]_V$, and T_{melt} . According to Kuwabara's^[27] study, only when $P_S = 2000$ Pa is the variation of $[\text{pct C}]_L$ in good agreement with the observed data, hence, a CO bubble radius of $r_{CO} = 1.8 \times 10^{-3}$ m can be extrapolated from the equation $P_S = 2\sigma/r_{CO}$. Bulk steel decarburization would not take place unless P_V drops to a certain level. Besides, the restriction on CO nucleation by P_h determines that CO is formed only in a shallow melt zone near the bath surface. The reaction rate (mass percent/s) is expressed as follows.

$$-\frac{d[\text{pct C}]_{in}}{dt} = \varphi \cdot \frac{A_V \cdot \rho_m \cdot k_{in}}{w} \times \int_0^{H_{in}} ([\text{pct C}]_V - [\text{pct C}]_{in}^e) dh_{CO} \quad [23]$$

The term $\int_0^{H_{in}} ([\text{pct C}]_V - [\text{pct C}]_{in}^e) dh_{CO}$ in Eq. [23] indicates that CO formation is the volume reaction taking place within a critical depth (H_{in}) under the bath surface. However, the zone occupied by Ar gas must be excluded from the total volume of the melt and Ar bubbles within H_{in} , for heterogeneous nucleation of CO bubbles occurs only in the liquid phase rather than in the gas phase. The value of H_{in} is determined by the difference between \underline{C} concentration ($[\text{pct C}]_V$) and equilibrium \underline{C} concentration ($[\text{pct C}]_{in}^e$), and $[\text{pct C}]_{in}^e$ mainly depends on the value of $P_V + \rho_m \cdot g \cdot h_{CO} + P_S$ as shown in Eq. [24].

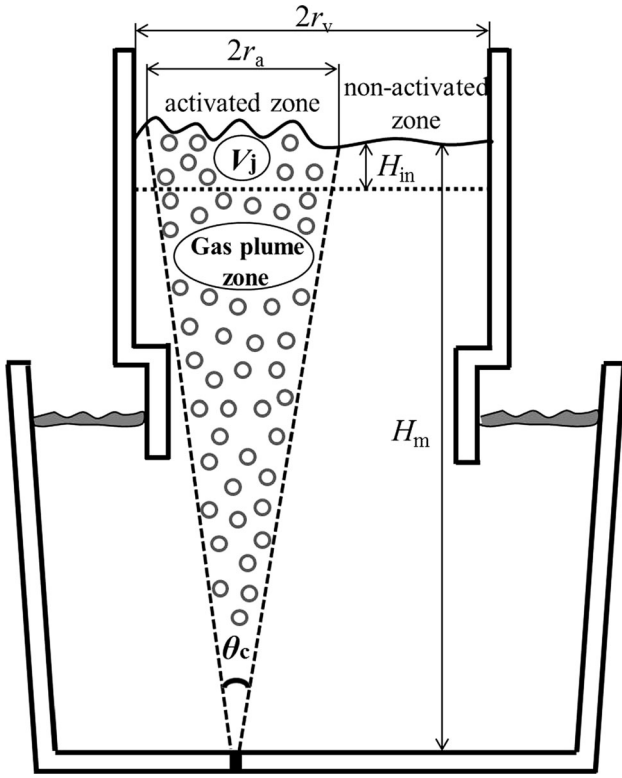


Fig. 6—Schematic diagram of gas plume zone in SSRF.

$$[\text{pct C}]_{\text{in}}^e = \frac{Pv + \rho_m \cdot g \cdot h_{\text{CO}} + P_s}{K \cdot f_c \cdot f_o \cdot [\text{pct O}]_V \cdot P^\theta} \quad [24]$$

1. Gas plume zone in molten steel

Figure 6 depicts the schematic diagram of gas plume zone in SSRF. The volume of gas plume zone is an important parameter directly influencing bulk steel decarburization efficiency, which is reflected from the value of ϕ (the volume fraction of molten steel within H_{in}), as expressed by Eq. [25]. In this model, ϕ has practical significance only on the premise of bulk steel decarburization taking place.

$$\phi = 1 - \frac{\lambda \cdot V_j}{\pi r_v^2 \cdot H_{\text{in}}}, \quad [25]$$

where λ is the ratio of the total Ar bubbles volume to the gas plume volume, and V_j is the gas plume volume within H_{in} . The zone occupied by Ar bubbles within H_{in} is considered to be non-nucleation zone.

It is essential to calculate the size of the gas plume zone for confirmation of V_j and λ . The upward cone angle of gas plume zone (θ_c) can be obtained by the following equation.^[28]

$$\frac{\theta_c}{180} = 0.915 Fr_m^{0.12} \cdot \left(\frac{H_m}{d_v}\right)^{-0.254} \cdot \left(\frac{d_0}{d_v}\right)^{0.441} \quad [26]$$

In Eq. [26], Fr_m is the modified Froude number which is determined by Eq. [27].

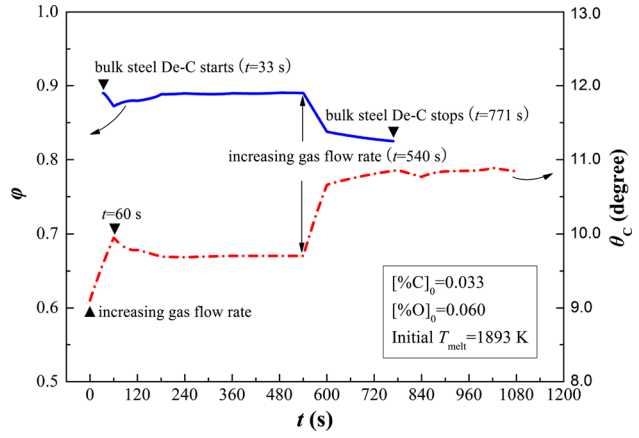


Fig. 7—Variations of ϕ and θ_c in the treatment process.

$$Fr_m = \frac{16G_{\text{Ar}}^2}{\pi^2 g \cdot d_0^4 \cdot H_m} \times \left(\frac{\rho_g}{\rho_m - \rho_g}\right) \quad [27]$$

It can be seen from Eqs. [26] and [27] that θ_c increases with the increase of G_{Ar} and the decrease of H_m . λ and V_j can be obtained through Eqs. [28] and [29], respectively.

$$\lambda = \frac{\sum_{p=1}^{N_L+N_V} 4\pi(r_b^p)^3 \cdot N_b^p/3}{\pi r_a^2 \cdot H_m/3} \quad [28]$$

$$V_j = \frac{1}{3}\pi \cdot \left(H_m \cdot \tan\left(\frac{\theta_c}{2}\right)\right)^2 \cdot H_m - \frac{1}{3}\pi \left((H_m - H_{\text{in}}) \cdot \tan\left(\frac{\theta_c}{2}\right)\right)^2 \cdot (H_m - H_{\text{in}}) \quad [29]$$

Figure 7 depicts variations of ϕ and θ_c in the treatment process. It can be seen that ϕ is in a range from 0.83 to 0.89, implying a fraction of 0.11 to 0.17 reduction of CO nucleation rate due to the existence of Ar gas in the bulk steel. On the other hand, θ_c fluctuates around an angle of 10 deg, and it varies oppositely to ϕ with time as shown in Figure 7, because V_j is inversely proportional to θ_c , as expressed in Eq. [29]. From the variation of ϕ , it can be easily seen that bulk steel decarburization starts at $t = 33$ seconds and ends at $t = 771$ seconds. In both ranges of $t = 33$ seconds to $t = 60$ seconds and $t = 540$ seconds to $t = 600$ seconds, ϕ shows a downward tendency due to the increase of gas flow rate (G_{Ar}) as shown in Figure 8(a).

2. Decarburization rate in the bulk steel

Based on the above calculations, the decarburization rate (kg/s) in the bulk steel can be obtained through the following equation.

$$V_{\text{in}} = \left(-\frac{d[\text{pct C}]_{\text{in}}}{100 \cdot dt}\right) \times w \quad [30]$$

E. Decarburization at the Bath Surface

Molten steel at the bath surface is violently stirred by the gas, greatly promoting contact between molten steel and the gas phase. Besides, CO being exhausted out of the vacuum vessel continuously facilitates bath surface decarburization. As the mechanism of bath surface decarburization is similar to that of Ar bubble surface decarburization, mass transfer of dissolved \underline{C} to the interface is also considered to be rate-determining step of bath surface decarburization. The reaction rate (mass percent/s) here is calculated by Eq. [31].

$$-\frac{d[\text{pct C}]_S}{dt} = \frac{A_S \cdot \rho_m \cdot k_S}{w} ([\text{pct C}]_V - [\text{pct C}]_S^e) \quad [31]$$

In Eq. [31], equilibrium \underline{C} concentration ($[\text{pct C}]_S^e$) mainly depends on CO partial pressure ($P_{\text{CO},V}$) in the vacuum vessel. It is calculated by Eq. [32].

$$[\text{pct C}]_S^e = \frac{P_{\text{CO},V}}{K \cdot f_C \cdot f_O \cdot [\text{pct O}]_V \cdot P^\theta} \quad [32]$$

1. Effective reaction area at the bath surface

Effective reaction area (A_S) is a key parameter to bath surface decarburization and largely determined by G_{Ar}

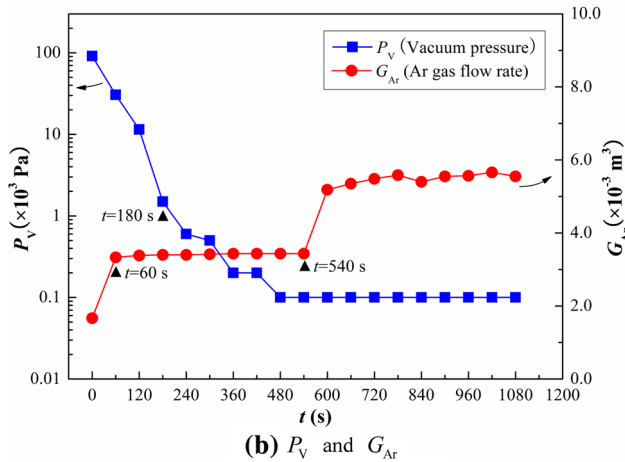
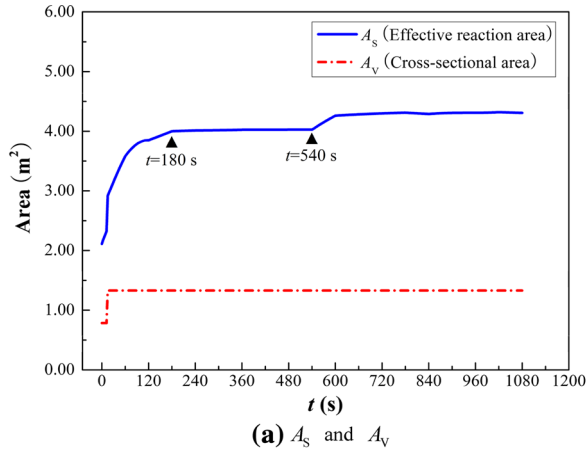


Fig. 8—Comparison between A_S and A_V under the designated P_V and G_{Ar} .

and P_V . In the present study, effect of slag on bath surface decarburization is neglected, and the bath surface is divided into two sections: non-activated zone and activated zone, as shown in Figure 6. The geometric area ($A_V - A_a$) of the non-activated zone is taken as its reaction area. In terms of the activated zone, since violent surface agitation is induced in the treatment process, especially when CO bubbles formation occurs vigorously at the early decarburization stage and when G_{Ar} increases at the slow decarburization stage, its effective area ($\xi \cdot A_a$) is much larger than the corresponding geometric area (A_a), and bath surface decarburization takes place mostly in the activated zone. Based on the above analysis, A_S is determined by Eq. [33].

$$A_S = (A_V - A_a) + \xi \cdot A_a \quad [33]$$

The difference between A_S and A_a depends on the activated coefficient (ξ) with respect to the activated zone at the bath surface. A range of ξ from 4.78 to 10.51 was obtained by Kitamura *et al.*^[29] based on the gas adsorption and desorption tests. In the present study, the intermediate value of the above range, $\xi = 7.5$, is determined as the activated coefficient of the activated zone. Figure 8 shows comparison between A_S and the geometric cross-sectional area of the bath surface (A_V) under the designated P_V and G_{Ar} .

It can be seen from Figure 8(a) that A_S increases significantly before $t = 180$ seconds due to the increase of G_{Ar} within the initial 60 seconds and the sharp decrease of P_V as shown in Figure 8(b). In addition, A_S shows a typical increase again at $t = 540$ seconds after a stable stage, which is also ascribed to the increase of G_{Ar} as shown in Figure 8(b). The cross-sectional area of the vacuum vessel A_V , by contrast, is apparently smaller than A_S due to the violent agitation induced by the gas plume in the activated zone. It is thus clear that both increasing G_{Ar} and accelerating the drop of P_V promote decarburization at the bath surface by enlarging the activated area.

2. Decarburization rate at the bath surface

Based on the above calculations, the decarburization rate (kg/s) at the bath surface is calculated by Eq. [34].

$$V_S = \left(-\frac{d[\text{pct C}]_S}{100 \cdot dt} \right) \times w \quad [34]$$

F. Parameters of the Model

The key parameters for the calculations of this model, including mass transfer coefficients of dissolved carbon to the interface (k_b , k_S), the process parameter (k_{in}), reaction area (A_{Ar} , A_V , A_S), the volume fraction of molten steel within the critical depth of CO nucleation (φ), and equilibrium partial pressure of CO ($P_{\text{CO},b}$, $P_{\text{CO},e}$, $P_{\text{CO},V}$), are listed in Table I. In the estimation of decarburization at Ar bubble surface, the interfacial area is the sum of all Ar bubbles in the melt, but decarburization for the bubbles at different heights is

Table I. Parameters of the Model

Ar Bubble Surface		Bulk Steel		Bath Surface	
k_b	$2 \left(\frac{D_C \cdot u_{\text{slip}}}{2\pi \cdot r_b} \right)^{1/2}$ ($u_{\text{slip}} = 0.63$ m/s)	k_{in}	20 s^{-1} process parameter	k_S	0.005 m/s
A_{Ar}	$\sum_{p=1}^{N_L+N_V} A_{\text{Ar}}^p$ $A_{\text{Ar}}^p = 4\pi(r_b^p)^2$ $r_b = 0.007$ to 0.031 m $r_{b,0} = 0.007$ to 0.008 m	A_V	$\begin{cases} \pi R_S^2, (H_V \leq 0.38\text{m}) \\ \pi r_V^2, (H_V > 0.38\text{m}) \end{cases}$	A_S	$(A_V - A_a) + \xi A_a$ ($A_S = 2.11$ to 4.31 m^2) $\xi = 7.5$ $A_a = \pi r_a^2$ ($r_a = 0.25$ to 0.38 m)
$P_{\text{CO},b}$	$\frac{n_{\text{CO}}^b}{n_{\text{Ar}}^b + n_{\text{CO}}^b} \times P_b$ $P_b = P_V + \rho_m g h_b + \frac{2\sigma}{r_b}$	$P_{\text{CO},e}$	$P_V + \rho_m g h_{\text{CO}} + P_S$ $h_{\text{CO}} \leq H_{\text{in}}, P_S = 2000\text{Pa}$	$P_{\text{CO},V}$	$\eta_{\text{CO}} \cdot P_V$
		φ	$1 - \frac{\lambda \cdot V_j}{\pi r_V^2 \cdot H_{\text{in}}}, (\varphi = 0.83 \text{ to } 0.89)$ $\lambda = \frac{\sum_{p=1}^{N_L+N_V} 4\pi(r_b^p)^3 \cdot N_b^p/3}{\pi r_V^2 \cdot H_m/3}$ $V_j = \frac{1}{3}\pi \left(r_a^2 H_m - (H_m - H_{\text{in}})^3 \tan^2\left(\frac{\theta_c}{2}\right) \right)$		

separately evaluated because the conditions (bubble size, CO partial pressure in the bubble, *etc.*) are constantly changing in the ascending process, so decarburization amount through Ar bubbles is obtained by summing up that from every single bubble. k_{in} is a process parameter for estimating CO nucleation rate in the bulk steel and $k_{\text{in}} \times dh_{\text{CO}}$ has the same dimension as that of mass transfer coefficients (k_b, k_S). The simulated results are in good agreement with industrial data when k_{in} is taken as 20 s^{-1} , as suggested by Kuwabara *et al.*^[27] Besides, the volume fraction of molten steel within H_{in} (φ) is in a range from 0.83 to 0.89. The mass transfer rate of dissolved C to the bath surface (k_S) is taken as 0.005 m/s in this model, which is larger than the value of 0.0015 m/s taken by Kitamura *et al.*^[1] for RH process. The difference with previous work may be ascribed to the dimension of the snorkel and Ar gas ascending distance in SSRF. The activated coefficient (ξ) is determined to be 7.5, and the radius of the activated zone (r_a) is in a range from 0.25 to 0.38 m that depends on the vacuum pressure (P_V) and gas flow rate (G_{Ar}). The equilibrium CO partial pressure ($P_{\text{CO},V}$) is determined by P_V and the fraction of CO in the vacuum chamber (η_{CO}).

G. Program and Computing Process

After developing the sub-models for three reaction sites, mathematical simulation of decarburization process in SSRF is performed by programming in Visual Basic 6.0 on a PC. The computational flow chart of decarburization process in SSRF is summarized in Figure 9. In the present calculations, the weight of molten steel (W_{melt}) is set to be 80,000 kg and the initial temperature of molten steel (T_{melt}) to be 1893 K (1620 °C); the initial mass content of dissolved carbon ([pctC]₀) and oxygen ([pctO]₀) is set to be 0.033 and 0.060, respectively; the decarburization cycle (t_{d-e}) is taken as 1080 seconds and the very short time step Δt is 0.06 seconds. With the above initial input conditions, the calculation results at any moment no later than 1080 seconds, including decarburization rate of each reaction site, the ratio of decarburization rate of each reaction site to the total decarburization rate, decarburization amount of each reaction site, the ratio of

decarburization amount of each reaction site to the total decarburization amount, the contents of dissolved C, Q, the temperature of molten steel, critical depth of CO nucleation in the bulk steel, effective reaction area at the bath surface, upward cone angle of gas plume, and the volume fraction of molten steel within H_{in} , can be output in a user-friendly interface.

III. RESULTS AND DISCUSSION

In the present study, a dynamic model has been developed to investigate decarburization behavior of an 80-ton SSRF by performing simulation of decarburization reactions that take place at Ar bubble surface, in the bulk steel and at the bath surface. The dimensions and process conditions of the SSRF system are listed in Table II.

As listed in Table II, the flow rate of argon gas (G_{Ar}) blown at the bottom of the ladle is in a range from 1.667×10^{-3} to $5.667 \times 10^{-3} \text{ m}^3/\text{s}$ in this model. It is also shown in Figure 8(b) that G_{Ar} increases to $3.33 \times 10^{-3} \text{ m}^3/\text{s}$ within the initial 60 seconds and then remains relatively stable until $t = 540$ seconds when G_{Ar} starts to increase again from 3.33×10^{-3} to $5.00 \times 10^{-3} \text{ m}^3/\text{s}$. After $t = 600$ seconds, G_{Ar} fluctuates in a small range from 5.00×10^{-3} to $5.667 \times 10^{-3} \text{ m}^3/\text{s}$. On the other hand, the vacuum pressure (P_V), with a fore vacuum of 91,200 Pa before the decarburization treatment, drops to 100 Pa within 480 seconds with a short stagnation from $t = 360$ seconds to $t = 420$ seconds. After $t = 480$ seconds, P_V maintains 100 Pa till the treatment end.

The circulation flow rate of molten steel (Q) is used to estimate the flow field and mixing characteristics of molten steel. Increasing Q promotes homogenization of steel between the ladle and the vacuum vessel. Yamaguchi *et al.*^[30] worked out the relationship between the volumetric mass transfer coefficient (ak_C) and Q , indicating that the increase of Q contributes to decarburization as shown in Eq. [35].

$$ak_C \propto A_V^{0.32} \times Q^{1.17} \times [\text{pct C}]^{1.48} \quad [35]$$

From Eq. [36], it is clear that ak_C increases with the increase of $Q^{1.17}$. Furthermore, Kuwabara *et al.*^[27]

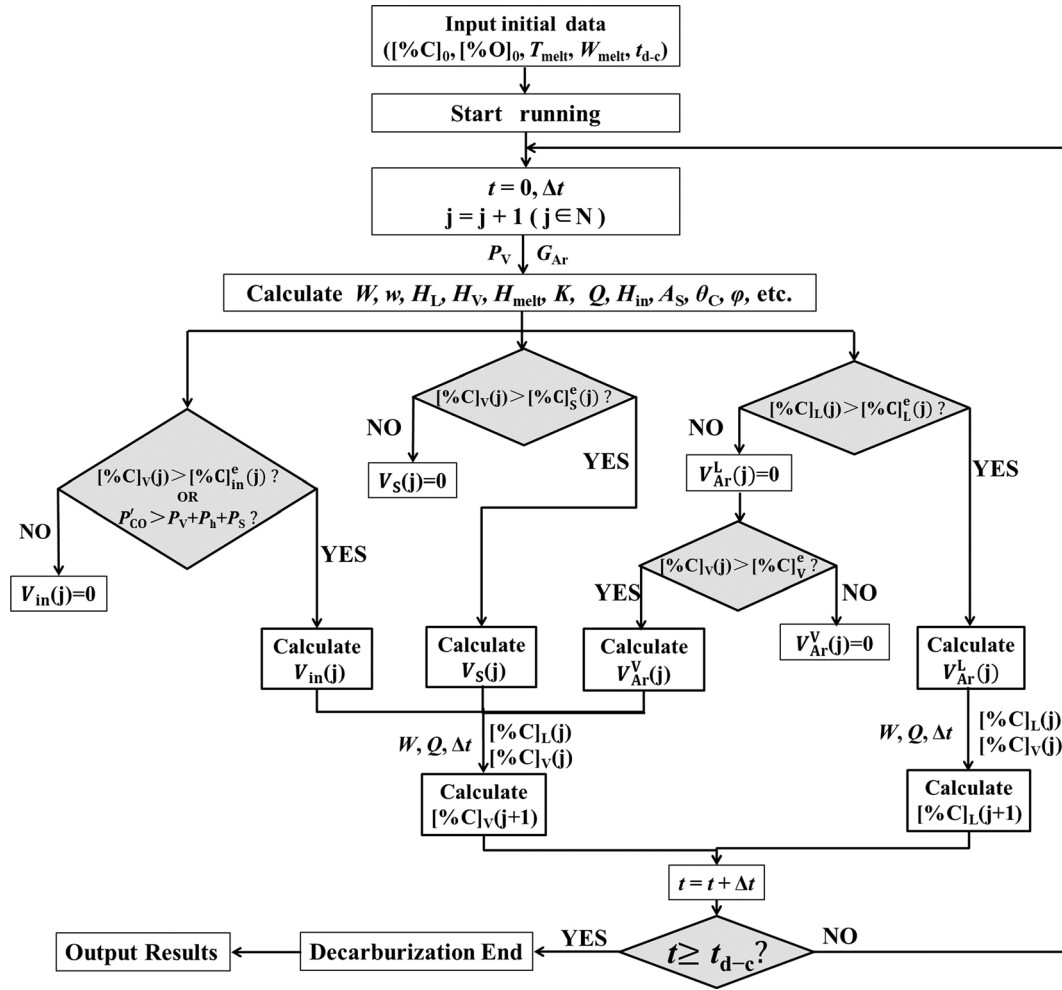


Fig. 9—Program flow chart for the decarburization process of SSRF.

Table II. Dimensions and Process Conditions of the 80-Ton SSRF System

Molten steel weight (kg)	80,000
Vacuum chamber	
Diameter (m)	1.300
Height (m)	8.700
Lift height (m)	1.435
Snorkel	
Diameter (m)	1.000
Height (m)	0.880
Immersion depth (m)	0.500
Ladle	
Upper diameter (m)	2.965
Lower diameter (m)	2.305
Height (m)	3.600
Gas injection system	
Gas type	Argon
Gas flow rate (m ³ /s)	1.667 to 5.667 × 10 ⁻³
Eccentric distance of the orifice (m)	0.500
Vacuum system	
Fore vacuum pressure (Pa)	91,200
Ultimate vacuum pressure (Pa)	≤100

deemed that Q is mainly affected by G_{Ar} , D_S , and P_V as shown in Eq. [36].

$$Q \propto G_{Ar}^{1/3} \cdot D_S^{4/3} \cdot \{\ln(P^0/P_V)\}^{1/3} \quad [36]$$

In order to investigate the circulation flow rate in SSRF, physical simulation^[5] was performed to investigate effects of the ratio of the snorkel diameter to the ladle diameter (D_S/D_L), the eccentricity of the porous plug (r_e/R_S), and G_{Ar} on Q . The relationship of them is summarized as follows.

$$Q \propto \left(-\left(\frac{D_S}{D_L}\right)^2 + 1.034 \cdot \left(\frac{D_S}{D_L}\right) \right) \times \left(-\left(\frac{r_e}{R_S}\right)^2 + 0.86 \cdot \left(\frac{r_e}{R_S}\right) \right) \times G_{Ar}^{0.3593} \quad [37]$$

By comparison between Eqs. [36] and [37], it can be seen that G_{Ar} has a greater impact on Q in SSRF than

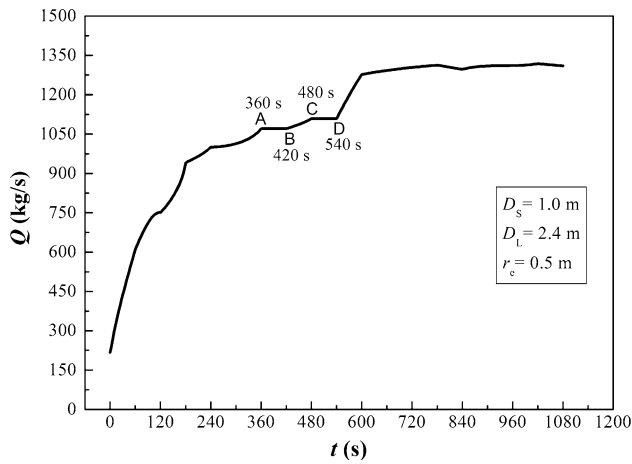


Fig. 10—Variation of Q in the decarburization process.

that in RH, due to a longer gas ascending distance in SSRF. In this model, previous results of both RH and SSRF were combined to estimate Q for the present 80-ton SSRF. With D_L , D_S , and r_c listed in Table II, the following formula was obtained to calculate Q .

$$Q = 4.45 \times 10^3 \cdot G_{Ar}^{0.3593} \cdot \{\ln(P^0/P_V)\}^{1/3} \quad [38]$$

Under G_{Ar} and P_V in Figure 8(b), variation of Q in the decarburization process is obtained as shown in Figure 10. It can be seen that Q increases from 216.67 to 1276.66 kg/s continuously within 600 seconds except for two staginations between $t = 360$ seconds and $t = 540$ seconds. After $t = 600$ seconds, Q fluctuates between 1276.66 and 1318.26 kg/s. In sum, Q can be improved by increasing G_{Ar} and reducing P_V .

In this model, the temperature of molten steel (T_{melt}) in the ladle is considered to be the same as that in the vacuum vessel. It is simulated according to the heat conservation law in SSRF process, as expressed in Eq. [39].

$$H_{in}^t - H_{out}^t = \int_{T_{melt}(t)}^{T_{melt}(t+\Delta t)} ((W+w) \cdot C_P^M + W_S \cdot C_P^S) \cdot dT_{melt} \quad [39]$$

Here, H_{in}^t is the reaction heat generated in the decarburization process during the time step Δt . During the decarburization treatment, there is little slag existing in the vacuum vessel and the temperature of molten steel is hardly influenced by the slag-steel reactions in the ladle, without O_2 blowing and Al addition during the decarburization period, so only the heat generated in C–O reaction (Eq. [1]) is taken as the source of H_{in}^t ; H_{out}^t is the heat loss that consists of loss for heating vacuum vessel when molten steel ascends into the vacuum vessel, loss through the waste gas, and loss dissipated from the ladle wall and the vacuum vessel wall to the air; $\int_{T_{melt}(t)}^{T_{melt}(t+\Delta t)} ((W+w) \cdot C_P^M + W_S \cdot C_P^S) \cdot dT_{melt}$ is the heat for heating (if $H_{in}^t - H_{out}^t > 0$) or refrigerating (if $H_{in}^t - H_{out}^t < 0$) molten steel and slag during Δt , which is equal to the

difference between heat intake H_{in}^t and heat loss H_{out}^t . Figure 11 shows variation of T_{melt} during the decarburization period. T_{melt} shows an apparent downward trend from 1893 K (1620 °C) to 1869 K (1596 °C) within the initial 123 seconds, and then decreases gradually to 1844 K (1571 °C) in the treatment end. In the beginning, molten steel gradually ascends into the vacuum vessel with the drop of P_V , the heat of molten steel was transferred to refractory of the vacuum vessel because of their temperature difference. When their temperature reaches a dynamic balance, T_{melt} falls more slowly, with heat loss of waste gas and heat dissipation through the slag, the ladle wall, and the vacuum vessel wall, though the C–O reaction heat is generated continuously.

Figure 12 shows comparison of $[pct C]_L$ between the simulated result and 27 heats plant data. The conditions (initial T_{melt} , $[pct C]_0$, $[pct O]_0$) of this model are consistent with those of the plant production. Obviously, the simulated $[pct C]_L$ varies within the range of $[pct C]_L$ in the plant production, that is, the simulated result is in reasonable agreement with actual production data, indicating that decarburization behavior in SSRF can be well explained by this model.

Variation of the simulated $[pct C]_L$ is divided into three stages: within the initial 51 seconds, $[pct C]_L$ decreases slowly from 0.033 to 0.031 at an average rate of 0.39 ppm/s; at the stage of $t = 51$ seconds to $t = 381$ seconds, $[pct C]_L$ decreases fast from 0.031 to 0.0079 at an average rate of 0.70 ppm/s; and at the stage of $t = 381$ seconds to $t = 1080$ seconds (the decarburization end), $[pct C]_L$ decreases more and more slowly from 0.0079 to 0.0014 at an average rate of only 0.093 ppm/s.

Figure 13 represents variation of decarburization rate at each site with the decrease of $[pct C]_L$. Decarburization rates at Ar bubble surface, at bath surface, and in the bulk steel are obtained from Eqs. [21], [30], and [34], respectively. It can be seen that decarburization reactions only take place at bath surface and Ar bubble surface at the beginning of treatment. When $[pct C]_L$ decreases to 0.0319 ($t = 33$ seconds), decarburization reaction starts in the bulk steel and its rate exceeds that at the bath surface at $t = 51$ seconds. In addition, in the range of $[pct C]_L$ from 0.031 ($t = 51$ seconds) to 0.0079 ($t = 381$ seconds), decarburization in the bulk steel predominates among three reaction sites. Meanwhile, the decarburization rates at both the bath surface and Ar bubble surface decrease gradually. After $t = 381$, the decarburization rate in the bulk steel starts to fall behind that at the bath surface and keeps up decreasing faster than those at the bath surface and Ar bubble surface. With $[pct C]_L$ further decreasing to about 0.005 at $t = 552$ seconds, the decarburization rate in the bulk steel is even smaller than that at Ar bubble surface, and the overall decarburization becomes weak. Obviously, decarburization occurs vigorously at the stage of $t = 51$ seconds to $t = 381$ seconds, when C concentration of molten steel is relatively high. Nevertheless, decarburization is slow before $[pct C]_L$ reduces to 0.031, because of high vacuum pressure limiting CO nucleation in the bulk steel. Compared with decarburization rates

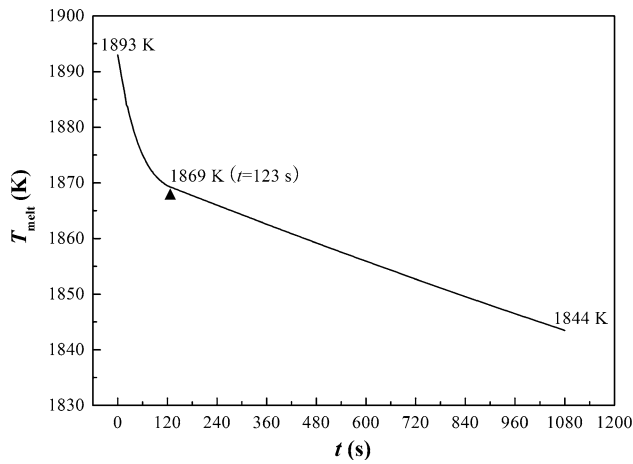


Fig. 11—Variation of T_{melt} during the decarburization period.

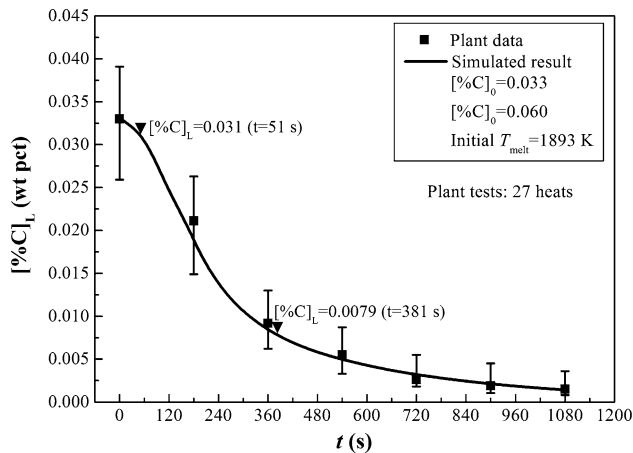


Fig. 12—Comparison of $[\text{pct C}]_L$ between the simulated result and plant data.

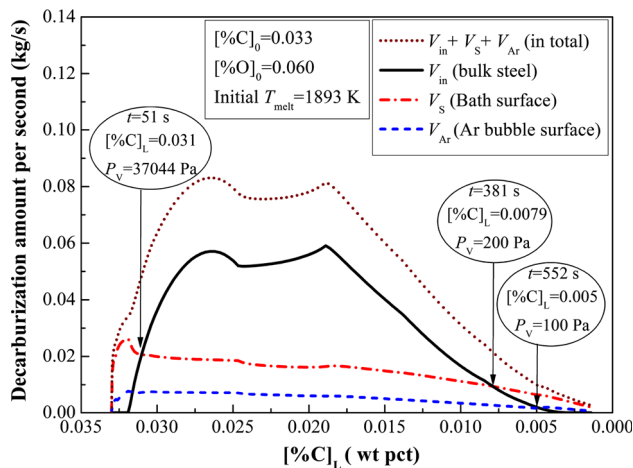


Fig. 13—Variation of decarburization rate with the decrease of $[\text{pct C}]_L$.

in the bulk steel and at the bath surface, decarburization rate at Ar bubble surface is much smaller over the whole decarburization process in SSRF. Besides, bulk steel

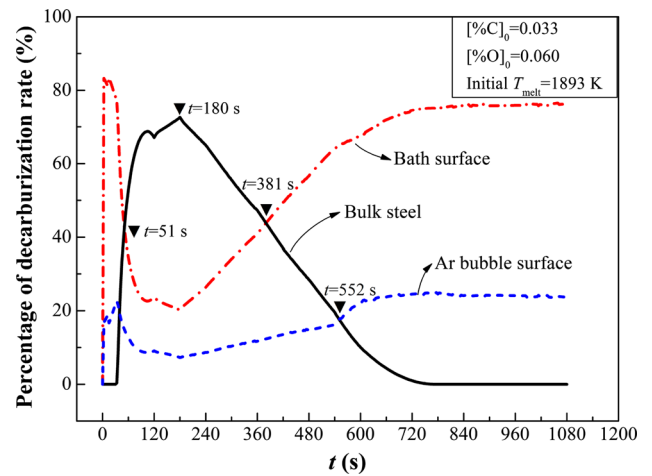


Fig. 14—Contributions of each decarburization rate to the total decarburization rate.

decarburization contributes the most to the total decarburization amount. Under the present conditions, the contributions of each decarburization amount are 50 pct by bulk steel decarburization, 37.1 pct by bath surface decarburization, and 12.9 pct by Ar bubble surface decarburization.

Figure 14 depicts the contributions of each decarburization rate to the total decarburization rate. It can be seen that decarburization rate at the bath surface takes up more than 80 pct of the total decarburization rate and the rest is from that at Ar bubble surface at the very first stage. However, once bulk steel decarburization starts, its contribution soon exceeds those of Ar bubble surface and the bath surface. In the period of $t = 51$ seconds to $t = 381$ seconds, the decarburization rate in the bulk steel accounts for over 43 pct of the total rate and peaks at 72.6 pct at $t = 180$ seconds. Since $t = 381$ seconds, the dominant reaction site has shifted to the bath surface with dramatic recession of CO nucleation in the bulk steel. Thereafter, the contribution of decarburization rate in the bulk steel continues decreasing, and decarburization mainly takes place at the bath surface and Ar bubble surface after $t = 552$ seconds when $[\text{pct C}]_L < 0.0050$.

In overall, the contribution of decarburization through heterogeneous nucleation of CO bubbles in the bulk steel contributes significantly to the decarburization process. Bulk steel decarburization predominates in the high carbon range. However, as the contents of dissolved $\underline{\text{C}}$, $\underline{\text{O}}$ decrease, the contribution of decarburization in the bulk steel decreases dramatically, and then decarburization at the bath surface plays a dominant role in the low carbon range. These results are basically consistent with previous work with respect to other steel making processes. Park *et al.*^[25] and Kitamura *et al.*^[31] proposed that bulk steel decarburization is dominant in the initial stage and the bath surface and Ar bubble surface reaction dominates the decarburization in the low carbon range in both RH process and REDA process.

As stated before, bulk steel decarburization occurs within a critical depth of H_{in} near the bath surface. The

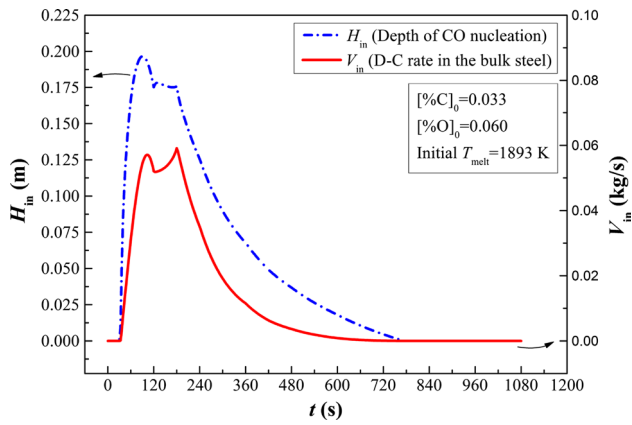


Fig. 15—Variations of H_{in} and V_{in} .

size of H_{in} determines the volume of molten steel participating in the reactions, which directly affects decarburization efficiency of SSRF. In the present study, H_{in} is obtained based on the critical balance between equilibrium CO partial pressure and $P_V + P_S$, as shown in Eq. [40].

$$H_{in} = \frac{K \cdot f_C \cdot f_O \cdot [\text{pct C}]_V \cdot [\text{pct O}]_V \cdot P^\theta - P_V - P_S}{\rho_m \cdot g} \quad [40]$$

Obviously, H_{in} is greatly influenced by $[\text{pct C}]_V$, $[\text{pct O}]_V$, and P_V . As $[\text{pct C}]_V$ and $[\text{pct O}]_V$ are high and P_V drops fast in the early period, H_{in} is great and CO bubbles are vigorously formed in the bulk steel. With $[\text{pct C}]_V$ and $[\text{pct O}]_V$ decreasing gradually during the treatment process, P_V plays a key role in determining the decarburization efficiency. Therefore, decarburization efficiency can be enhanced by keeping up a high drop rate of P_V . By substituting Eq. [40] into Eqs. [23] and [30], the decarburization rate in the bulk steel (V_{in}) can be expressed as follows.

$$V_{in} = \varphi \cdot \frac{A_V \cdot k_{in} \cdot \rho_m^2 \cdot g}{200 \cdot K \cdot f_C \cdot f_O \cdot [\text{pct O}]_V \cdot P^\theta} \times H_{in}^2 \quad [41]$$

As shown in Eq. [41], the decarburization rate in the bulk steel is in direct proportion to the second power of H_{in} . Figure 15 shows the variations of V_{in} and H_{in} . It can be seen that H_{in} has almost the same variation tendency as V_{in} . Besides, there is a peak and a platform of H_{in} as shown in dotted line of Figure 15. The reason for the transition from the peak to the platform of H_{in} is that the drop rate of P_V falls behind in that of $[\text{pct C}]_V$. Meanwhile, the trough to the second peak of V_{in} depicted with solid line is caused by sustained reduction of $[\text{pct O}]_V$ when H_{in} is practically unchanged, with reference to Eq. [41]. Hence it is clear that decarburization in the bulk steel is largely influenced by P_V . Accelerating the drop of P_V improves decarburization efficiency by expanding CO nucleation zone, especially when the contents of dissolved \underline{C} , \underline{O} are high in the early decarburization period.

Figure 16 shows the variations of decarburization rates at the bath surface (V_S) and Ar bubble surface (V_{Ar}). An improvement in both V_S and V_{Ar} can be seen

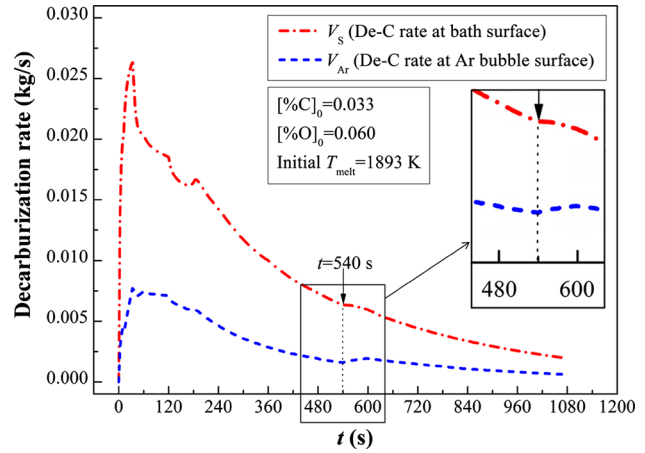


Fig. 16—Variations of V_S and V_{Ar} .

from the curves in the square frame at $t = 540$ seconds when G_{Ar} shows a typical upward trend as shown in Figure 8(b). However, it is actually not advisable that G_{Ar} be as high as possible when CO formation takes place vigorously in the bulk steel before $t = 381$ seconds, for a significant increase in G_{Ar} will cause a decrease in φ , as indicated in Figure 7. Only when bulk steel decarburization becomes very slightly ($[\text{pct C}]_L < 0.005$), and meanwhile CO gas is mostly formed at the bath surface and Ar bubble surface, is increasing G_{Ar} an effective measure to be taken to improve decarburization efficiency by expanding activated area of the bath surface (as shown in Figure 8) and the total surface area of Ar bubbles. Besides, circulation flow rate of SSRF will also be enhanced by the increase of G_{Ar} to accelerate mass transfer of dissolved \underline{C} , \underline{O} to the reaction interface.

IV. SUMMARY AND CONCLUSIONS

Single snorkel refining furnace is a new-type refining equipment applied to deep decarburization treatment of ultra-low carbon steel. In order to further improve decarburization efficiency and provide probable guidance for industrial scale production in SSRF, a dynamic model has been developed to investigate decarburization behavior by programming in Visual Basic 6.0 on a PC and the simulated result is in reasonable agreement with the plant data. In this model, decarburization reactions are considered to take place at Ar bubble surface, in the bulk steel and at the bath surface. Within the initial 51 seconds, $[\text{pct C}]_L$ decreases slowly from 0.033 to 0.031 at an average rate of 0.39 ppm/s and bath surface decarburization contributes the most to the total decarburization; at the stage of $t = 51$ seconds ($[\text{pct C}]_L = 0.031$) to $t = 381$ seconds ($[\text{pct C}]_L = 0.0079$), $[\text{pct C}]_L$ decreases fast at an average rate of 0.70 ppm/s, in which bulk steel decarburization occurs vigorously under a sharp decrease of P_V and it predominates in the overall decarburization; and at the stage of $t = 381$ seconds ($[\text{pct C}]_L = 0.0079$) to the decarburization end ($[\text{pct C}]_L = 0.0014$), $[\text{pct C}]_L$ reduces more and more

slowly at an average rate of only 0.093 ppm/s, in which the dominant decarburization site has shifted to the bath surface after a dramatic recession of bulk steel decarburization. Throughout the decarburization process, the contributions of each decarburization amount are 50 pct by bulk steel decarburization, 37.1 pct by bath surface decarburization, and 12.9 pct by Ar bubble surface decarburization.

When decarburization takes place vigorously in the bulk steel before $t = 381$ seconds ($[\text{pct C}]_L > 0.0079$), too high G_{Ar} is inadvisable. In the early period when the contents of dissolved $\underline{\text{C}}$, $\underline{\text{O}}$ are relatively high, to accelerate the drop of P_V is an effective way to improve decarburization efficiency by deepening the depth of CO nucleation in the bulk steel. Besides, when decarburization becomes very slow after $t = 552$ seconds ($[\text{pct C}]_L < 0.0050$), it is necessary to appropriately increase G_{Ar} to slow down the reduction of decarburization rate by expanding activated area of the bath surface and the total surface area of Ar bubbles.

ACKNOWLEDGMENTS

The authors would like to thank Shanxi Stainless Steel Corporation Limited for providing the actual production data and also appreciate the assistance of some companies for providing the Visual Basic 6.0 software.

NOMENCLATURE

ak_C	Volumetric mass transfer coefficient of $\underline{\text{C}}$ in molten steel (m^3/s)
A_{Ar}	Surface area of an Ar bubble (m^2)
A_a, A_s, A_v	Activated area, effective reaction area, cross-sectional area of the bath surface (m^2)
C_g, C_p^S, C_p^M	Heat capacity of Ar gas, metal, slag ($\text{J}/\text{kg K}$)
[pct i]	Mass concentration of component i (weight percent)
[pct i] ^e	Equilibrium concentration of component i (weight percent)
d_0, d'_0	Hole diameter of the porous plug (mm, cm)
$d_{b,0}, d_b$	Initial Ar bubble diameter, Ar bubble diameter in the ascending process (cm, m)
d_v	Diameter of bath surface in the vacuum vessel (m)
D_C	Diffusion coefficient of dissolved $\underline{\text{C}}$ in molten steel (m^2/s)
D_S, D_L	Diameter of the snorkel, ladle (m)
f_i	Activity coefficient of component i in molten steel

g', g	Acceleration of gravity ($\text{cm}/\text{s}^2, \text{m}/\text{s}^2$)
$G'_{\text{Ar}}, G_{\text{Ar}}$	Ar gas flow rate ($\text{cm}^3/\text{s}, \text{m}^3/\text{s}$)
h_b, h_{CO}	Distance from position of Ar bubble, CO nucleation site to the bath surface (m)
H_{in}	Critical depth of CO nucleation in the bulk steel (m)
H_L, H_V	The bath depth in the ladle, vacuum vessel (m)
H_m	Distance from the porous plug to the bath surface (m)
$H'_{\text{in}}, H'_{\text{out}}$	Generated decarburization reaction heat, heat loss within time step Δt (J)
K	Equilibrium constant of decarburization reaction
k_b, k_s	Mass transfer coefficient of $\underline{\text{C}}$ to Ar bubble surface, the bath surface (m/s)
k_{in}	Process parameter of bulk steel decarburization (s^{-1})
M_i	Atomic weight of component i (g/mol)
$n_{\text{Ar}}^b, n_{\text{CO}}^b$	The number of moles of Ar, CO in the Ar bubble (mol)
N_b	The number of Ar bubble whose radius is r_b
N_h	The number of holes of the porous plug
N_L, N_V	The number of Ar bubbles in the ladle, vacuum vessel
P_0, P_b	Pressure at the porous plug, Ar bubble inside (P_a)
P^θ	Standard atmospheric pressure ($P^\theta = 101325 P_a$)
P_{CO}	CO partial pressure at the interface (P_a)
$P_{\text{CO,in}}, P_{\text{CO,b}}, P_{\text{CO,v}}$	Equilibrium CO partial pressure in the bulk steel, Ar bubble, vacuum vessel (P_a)
P_S	Evolution pressure of CO bubble in the bulk steel (P_a)
P_V, P_h	Vacuum pressure, hydrostatic pressure of molten steel (P_a)
Q	Circulation flow rate of molten steel (kg/s)
r_a, r_v	Radius of activated bath surface, bath surface (m)
$r_{b,0}, r_b$	Initial Ar bubble radius, Ar bubble radius in the ascending process (m)
r'_b, r''_b	The first, second derivative of Ar bubble radius to time ($\text{m}/\text{s}, \text{m}/\text{s}^2$)
r_{CO}	Critical CO nucleation radius (m)
r_e	Eccentric distance of the orifice (m)
R_S	The inner radius of the snorkel (m)
t	Treatment time (s)
t_b	Ar bubble ascending time (s)

T_0, T, T_{melt}	The temperature of Ar gas at the porous plug, Ar bubble, molten steel (K)
u_{slip}	Relative velocity of Ar bubble (m/s)
u_{b}	Bubble ascending velocity, $u_{\text{b}} = u_{\text{slip}} + 2Q/\pi(D_S/2)^2$ (m/s)
$V_{\text{Ar}}^{\text{L}}, V_{\text{Ar}}^{\text{V}}, V_{\text{in}}, V_{\text{S}}$	Decarburization rate at Ar bubble surface of the ladle, Ar bubble surface of the Vacuum vessel, the bulk steel, the bath surface (kg/s)
V_{g}	The volume of an Ar bubble (m^3)
V_{j}	Volume of gas plume within the critical depth of CO nucleation (H_{in}) (m^3)
W, w, W_{S}	Steel weight in the ladle, steel weight in the vacuum vessel, slag weight (kg)
σ, σ'	Surface tension of molten steel ($\sigma = 1.8 \text{ N/m}, \sigma' = 1800 \text{ dyn/cm}$)
ρ_{g}	Density of Ar gas (kg/m^3)
$\rho_{\text{m}}, \rho'_{\text{m}}$	Density of molten steel ($\text{kg/m}^3, \text{g/cm}^3$)
α	A constant ($\alpha = 30$)
μ	Viscosity of molten steel ($\mu = 5.8 \times 10^{-3} \text{ N s/m}^2$)
ψ	Heat transfer coefficient of Ar gas ($\text{W/m}^2 \text{ K}$)
ξ	Activated coefficient of the bath surface
φ	The volume fraction of molten steel within H_{in} ($\varphi < 1$)
λ	Volume fraction of Ar gas in the gas plume
θ_{C}	Upward cone angle of the gas plume (deg)
η_{CO}	The fraction of CO in the vacuum chamber
Δt	Time step (s)
i, j	Component i, j dissolved in molten steel
L, V, in, S	Ladle vacuum vessel, bulk steel, bath surface
$m(1, 2, \dots, N_{\text{L}})$	Serial number of bubble from the bottom of ladle to bath surface of the ladle
$n(1, 2, \dots, N_{\text{V}})$	Serial number of bubble from bath surface of the ladle to that of the vacuum vessel
$p(1, \dots, N_{\text{L}} + N_{\text{V}})$	Serial number of bubble from the porous plug to bath surface of the vacuum vessel

REFERENCES

1. S. Kitamura, M. Yano, K. Harashima, and N. Tsutsumi: *Tetsu-to-Hagané*, 1994, vol. 80 (3), pp. 213–18.
2. V. Seshadri, C.A. da Silva, I.A. da Silva, G.A. Vargas P.S.B. Lascosqui: *Ironmak Steelmak*, 2006, vol. 33 (1), pp. 34–38.
3. B.S. Liu, G.S. Zhu, B.H. Li, B.H. Li, Y. Cui, and A.M. Cui: *Int. J. Miner. Metall. Mater.*, 2010, vol. 17 (1), pp. 22–27.
4. J. Zhang: *Dali. Spec. Steel*, 1978, vol. 3 (1), pp. 5–26.
5. Z. Qin: Ph.D. Dissertation, University of Science and Technology Beijing, Beijing, China, 2010 pp. 70–73.
6. J.P. Duan, Y.L. Zhang, X.M. Yang, G.G. Cheng, and J. Zhang: *Spec. Steel*, 2012, vol. 33 (1), pp. 26–29.
7. G.G. Cheng, J. Zhang, N.Z. Yang, and F.S. Tong: *Spec. Steel*, 1994, vol. 15 (5), pp. 22–25.
8. J. Zhang, G.G. Cheng, N.Z. Yang, and F.S. Tong: *Iron Steel*, 1995, vol. 30 (5), pp. 19–21.
9. G.G. Cheng, J. Zhang, F.S. Tong, and X.J. Yi: *Spec. Steel*, 1994, vol. 15 (1), pp. 27–30.
10. Z. Qin, M.T. Zhu, G.G. Cheng, and J. Zhang: *Spec. Steel*, 2010, vol. 31 (5), pp. 5–7.
11. X.M. Yang, M. Zhang, F. Wang, J.P. Duan, and J. Zhang: *Steel. Res. Int.*, 2012, vol. 83 (1), pp. 55–82.
12. Q.X. Rui and G.G. Cheng: *Adv. Mater. Res.*, 2012, vols. 476–478, pp. 340–45.
13. Q.X. Rui, F. Jiang, Z. Ma, Z.M. You, G.G. Cheng, and J. Zhang: *Steel Res. Int.*, 2013, vol. 84 (2), pp. 192–97.
14. J.P. Duan, Y.L. Zhang, X.M. Yang, G.G. Cheng, and J. Zhang: *Steelmaking*, 2011, vol. 27 (6), pp. 44–48.
15. J.P. Duan, Y.L. Zhang, X.M. Yang, G.G. Cheng, J. Zhang, and H.J. Guo: *Iron Steel*, 2011, vol. 46 (7), pp. 21–25.
16. J.Y. Zhang: *Physical Chemistry of Metallurgy*, 1st ed., Metallurgical Industry Press, Beijing, 2009, pp. 45–48, 214–16.
17. S. Inoue, Y. Furuno, T. Usui, and S. Miyahara: *ISIJ Int.*, 1992, vol. 32 (1), pp. 120–25.
18. H. Saint-Raymond, D. Huin, and F. Stouvenot: *Mater. Trans. JIM*, 2000, vol. 41 (1), pp. 17–21.
19. J.F. Domgin, P. Gardin, H. Saint-Raymond, F. Stouvenot, and D. Huin: *Steel Res. Int.*, 2005, vol. 76 (1), pp. 5–12.
20. M.A.V. Ende, Y.M. Kin, M.K. Cho, J. Choi, and I.H. Jung: *Metall. Mater. Trans. B*, 2011, vol. 42B, pp. 477–89.
21. R. Higbie: *Trans. Am. Inst. Chem. Eng.*, 1935, vol. 31, pp. 365–89.
22. V.G. Levich: *Physicochemical Hydrodynamics*, Prentice-Hall Inc., Englewood Cliffs, 1962, pp. 452–54.
23. M. Sano, K. Mori, and T. Sato: *Tetsu-to-Hagané*, 1977, vol. 63 (14), pp. 42–49.
24. J. Szekely and G.P. Martins: *Trans. Am. Soc. Metal.*, 1969, vol. 245, pp. 629–36.
25. Y.G. Park and K.W. Yi: *ISIJ Int.*, 2003, vol. 43 (9), pp. 1403–1409.
26. F.D. Richardson: *Physical Chemistry of Melts in Metallurgy*, 1st ed., vol. 2, Academic Press, London, 1974, pp. 457–60.
27. T. Kuwabara, K. Umezawa, K. Mori, and H. Watanabe: *Trans. ISIJ*, 1988, vol. 28, pp. 305–14.
28. G.G. Krishna Murthy, A. Ghosh, and S.P. Mehrotra: *Metall. Trans. B*, 1988, vol. 19B, pp. 885–92.
29. S. Kitamura, K. Miyamoto, and R. Tsujino: *Tetsu-to-Hagané*, 1994, vol. 80 (2), pp. 101–106.
30. K. Yamaguchi, Y. Kishimoto, T. Sakuraya, T. Fujii, and M. Aratani: *ISIJ Int.*, 1992, vol. 32 (1), pp. 126–35.
31. S. Kitamura, H. Aoki, K. Miyamoto, H. Furuta, K. Yamashita, and K. Yonezawa: *ISIJ Int.*, 2000, vol. 40 (5), pp. 455–59.